RSC Advances

PAPER

View Article Online
View Journal | View Issue

Cite this: *RSC Adv.*, 2025, **15**, 6962

Smart fluorometric sensing of metal contaminants in canned foods: a carbon dot-based dual-response system for quantifying aluminum and cobalt ions†

Al-Montaser Bellah H. Ali, *[a] Mohamed R. Elmasry,[b] Yousef A. Bin Jardan[c] and Mohamed M. El-Wekil[a]

The leaching of aluminum and cobalt ions into canned foods, such as aluminum from canned tomato sauce and cobalt from canned tuna, raises concerns about potential health risks, making their accurate detection essential for food safety. In this study, we developed a novel ratiometric fluorometric sensor based on dual-emission carbon dots capable of selectively detecting aluminum (Al^{3+}) and cobalt (Co^{2+}) ions after a single excitation. The sensor exhibits distinct fluorescence responses: cobalt ions enhance the emission at 403 nm due to interactions with nitrogen and sulfur groups on the carbon dot surface, while Al^{3+} enhance the emission at 532 nm through binding with oxygen-rich groups such as carboxyl and hydroxyl. This differential response stems from the varying affinities of these metal ions for different functional groups, as confirmed through mechanistic studies and comprehensive characterization of the carbon dots, including TEM, UV-Vis, FTIR, and fluorescence lifetime analyses. The method demonstrates excellent sensitivity, with limits of detection (LOD) of 0.012 μM for Co^{2+} and 0.06 μM for Al^{3+}. The sensor's performance was validated with real food samples, successfully determining Al^{3+} in canned tomato sauce and Co^{2+} in canned tuna. The method exhibited high selectivity with minimal interference, achieving recovery rates of 97.50–100.67% for Al^{3+} and 97.01–98.02% for Co^{2+}. These findings underscore the robustness and practical applicability of the proposed sensor as a reliable tool for monitoring Al^{3+} and Co^{2+} in canned foods, ensuring food safety and compliance with regulatory standards.

Received 19th January 2025
Accepted 25th February 2025

DOI: 10.1039/d5ra00448a

rsc.li/rsc-advances

1. Introduction

The presence of metal ions such as aluminum and cobalt in canned and packaged food products has raised significant concerns regarding food safety and public health. Aluminum ions are commonly found in foods like canned tomatoes, orange juice, lemon juice, pickles, and energy drinks due to their interaction with aluminum-based packaging or linings, especially under acidic or high-salt conditions.[1] Similarly, cobalt ions can leach into food products such as canned fish or tuna, energy drinks, canned tomatoes, pickled vegetables, and beverages stored in blue glass bottles or ceramic containers with cobalt-based glazes and coatings.[2,3] The levels of these ions in food are influenced by several factors, including the acidity, salt content, and fat composition of the food, as well as storage conditions like temperature, duration, and the integrity of protective linings.[4] The presence of aluminum and cobalt ions in food products poses potential health risks, such as neurotoxicity, cardiomyopathy, thyroid dysfunction, and oxidative stress, as well as possible impacts on food quality and shelf life.[5,6] Determining the levels of these ions in various food products is essential to ensure compliance with regulatory standards, assess the safety of food packaging materials, and minimize the risks associated with long-term exposure. This study aims to address these concerns by analyzing the presence of aluminum and cobalt ions in selected food matrices and exploring the factors that contribute to their migration into food.

Over the years, various methods have been developed for the determination of cobalt and aluminum ions in food products. These include spectroscopic techniques such as atomic absorption spectroscopy (AAS),[7,8] inductively coupled plasma optical emission spectroscopy,[9] and inductively coupled plasma mass spectrometry (ICP-MS).[10] These methods offer high sensitivity and accuracy, making them suitable for detecting trace amounts of these ions. Electrochemical methods, including anodic stripping voltammetry and differential pulse voltammetry, have also been utilized, particularly for their portability and relatively low cost.[11,12] Additionally, colorimetric

[a]Department of Pharmaceutical Analytical Chemistry, Faculty of Pharmacy, Assiut University, Assiut, Egypt. E-mail: Almontaser_bellah@aun.edu.eg
[b]School of Chemical Engineering, Sungkyunkwan University (SKKU), Suwon 16419, Republic of Korea
[c]Department of Pharmaceutics, College of Pharmacy, King Saud University, Riyadh, Saudi Arabia

† Electronic supplementary information (ESI) available. See DOI: https://doi.org/10.1039/d5ra00448a

assays using specific chelating agents have been employed for simpler, more rapid detection.[13,14] However, these methods come with limitations. Spectroscopic techniques like ICP-MS and AAS require expensive instrumentation, extensive sample preparation, and trained personnel, making them less accessible for routine or on-site analysis. Electrochemical methods, while cost-effective, often suffer from matrix interferences, particularly in complex food samples, leading to reduced selectivity and reliability. Colorimetric methods, though convenient, are prone to interference from other ions or organic compounds present in food, which can lead to false positives or inaccurate quantification. Moreover, many traditional methods lack the capability for simultaneous detection of multiple ions in a single analysis, increasing the time and resources required for comprehensive testing. These limitations highlight the need for innovative approaches that are not only sensitive and selective but also capable of real-time and cost-effective detection of cobalt and aluminum ions in diverse food matrices.

Carbon dots (CDs) have emerged as promising fluorescence sensors for metal ion detection due to their unique optical properties, high sensitivity, and ease of functionalization.[15,16] These nanoscale carbon-based materials exhibit strong fluorescence, good biocompatibility, and resistance to photobleaching, making them ideal for analytical applications.[17,18] Functional groups on the surface of CDs can be tailored to selectively bind specific metal ions, causing measurable fluorescence changes such as quenching, enhancement, or shifts in emission wavelengths.[19–21] This allows CDs to act as highly selective and sensitive detectors for various metal ions, even at trace levels. Their potential for rapid, cost-effective, and portable sensing makes them a valuable tool for environmental monitoring, food safety, and biomedical applications.[22]

Canned tomatoes are an excellent choice for investigating Al^{3+} levels due to their highly acidic nature (pH ~4.0–4.5), which accelerates aluminum leaching from can linings, and their widespread consumption, making them relevant for public health studies.[4] Similarly, canned tuna is ideal for studying Co^{2+} levels as it is typically packaged in steel cans that may contain cobalt alloys or coatings, and its fat content can interact with cobalt, providing a practical matrix for migration studies.[23] Both matrices are supported by literature and offer real-life exposure scenarios, with canned tomatoes highlighting aluminum migration in acidic foods and canned tuna addressing cobalt contamination from packaging and environmental sources.[2,24,25]

This study introduces a novel nitrogen and sulfur doped dual-emission carbon dot (NSDC-dots) based fluorescence sensor for the determination of cobalt and aluminum ions in canned food products. The sensor exhibits selective fluorescence responses, with cobalt ions enhancing the emission peak at 403 nm while leaving the 532 nm peak unaffected, and aluminum ions selectively enhancing the 532 nm peak without altering the 403 nm emission. This unique behavior enables ratiometric fluorometric determination of either ion individually and simultaneous quantification of both ions using the same probe. Unlike existing methods, this is the first fluorometric approach specifically applied to the detection of aluminum and cobalt ions in canned food products, providing a rapid, sensitive, and selective solution to address food safety concerns.

2. Experimental

2.1. Materials and reagents

Lactic acid, benzoic acid, saccharin, *o*-phenylene diamine (OPD), sodium hydroxide, phosphoric acid, glacial acetic acid, boric acid, aluminum sulfate ($Al_2(SO_4)_3$), copper sulfate ($CuSO_4$), ferric chloride ($FeCl_3$), cobalt chloride ($CoCl_2$), zinc nitrate ($Zn(NO_3)_2$), and manganese chloride ($MnCl_2$) were procured from Sigma-Aldrich (Steinheim, Germany). Glucose, sucrose, fructose, glycine, histidine, cysteine, citric acid, ascorbic acid, nickel sulfate ($NiSO_4$), chromium nitrate ($Cr(NO_3)_3$), sodium chloride (NaCl), potassium nitrate (KNO_3), magnesium sulfate ($MgSO_4$), calcium phosphate ($Ca_3(PO_4)_2$), calcium sulfate ($CaSO_4$), sodium nitrate ($NaNO_3$), potassium sulfate (K_2SO_4), magnesium chloride ($MgCl_2$), and aluminum phosphate ($AlPO_4$) were procured from El-Nasr Pharmaceutical Chemicals Co., Cairo, Egypt. Throughout the experiments, ultra-pure water with a resistivity of 18.2 MΩ cm was utilized.

2.2. Instrumentation and characterization

Detailed explanations of the procedures and calculations can be found in the ESI file.†

2.3. Preparation of NSDC-dots

The preparation of NSDC-dots involved solvothermal synthesis using cysteine (65 mg) and *o*-phenylenediamine (200 mg) as starting materials dissolved in 10 mL ethanol. The mixture was initially subjected to sonication to achieve homogeneous dispersion, followed by transfer to an autoclave with Teflon lining where it underwent thermal processing at 180 °C maintained for 6 hours. After allowing the reaction vessel to cool down to ambient temperature naturally, the product underwent multiple purification stages. These included initial filtration through a membrane (0.22 μm pore size) to remove larger particulates, followed by extensive dialysis over 24 hours using a membrane with 1 kDa molecular weight cutoff to eliminate any unreacted precursors and small molecular weight impurities. Finally, the purified carbon dots were obtained in powder form through freeze-drying and stored in refrigerated conditions (4 °C) for subsequent use in various characterization and application studies (Scheme 1).

2.4. Fluorescence quantum yields measurement of NSDC-dots

Detailed explanations of the procedures and calculations can be found in the ESI file.†

2.5. Fluorescence detection of Co^{2+} and Al^{3+}

The metal ion detection experiments utilized synthesized NSDC-dots under optimized conditions for each ion. For Co^{2+} detection, 0.5 mL of NSDC-dots (0.5 mg mL^{-1}) was mixed with

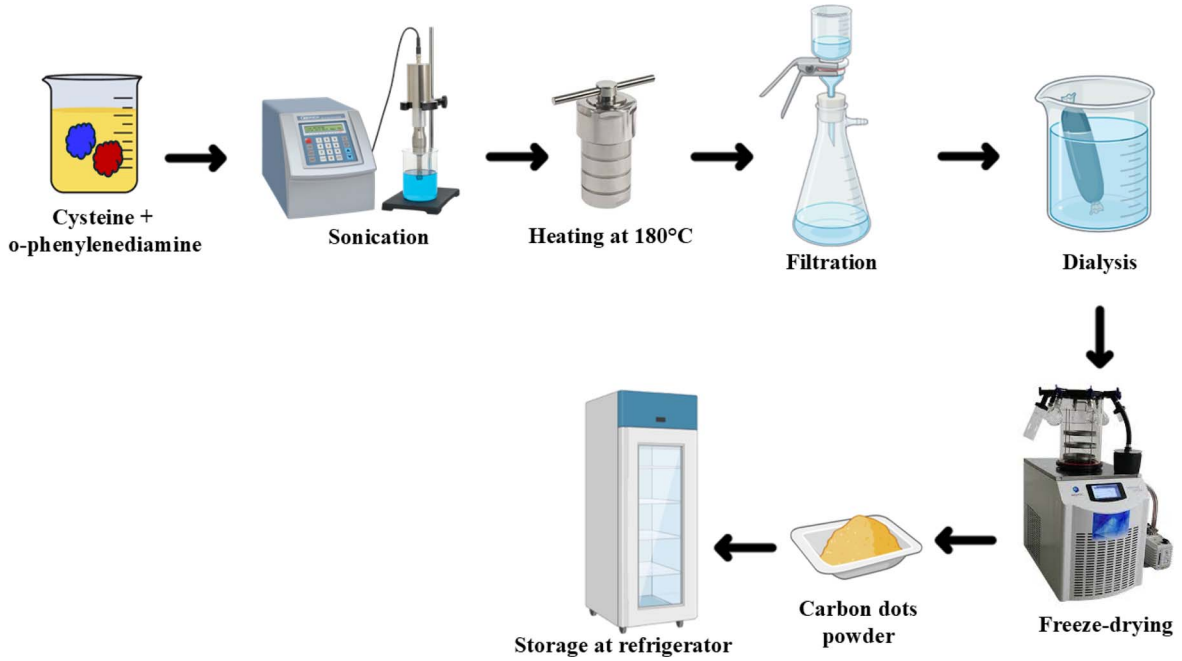

Scheme 1 Steps for preparing NSDC-dots.

2.0 mL of Britton–Robinson (BR) buffer (pH 7.0), followed by the addition of 2.0 mL of varying Co^{2+} concentrations. Similarly, Al^{3+} detection involved 0.5 mL of NSDC-dots (0.5 mg mL^{-1}) combined with 2.0 mL of BR buffer (pH 4.0), followed by Al^{3+} addition (2.0 mL). Both mixtures equilibrated at room temperature for 1 min before dilution to 10 mL with ultra-pure water. Fluorescence measurements were conducted at 320 nm excitation, with ratiometric responses recorded as F_{403}/F_{532} for Co^{2+} and F_{532}/F_{403} for Al^{3+}, ensuring selective detection.

2.6. Canned tomatoes sample preparation for Al^{3+} determination

Canned tomatoes were purchased from Egyptian supermarkets (Assiut City, Egypt), with expiration dates spanning from the first month to two years at the time of analysis. Three samples were taken from three cans sharing the same batch number to ensure consistency in the study. For the extraction of Al^{3+} from canned tomatoes, the entire content of each can was homogenized using a blender, and a 20.0 g aliquot was taken for analysis while the remaining was frozen at −20 °C for further use. The following extraction steps were adopted from a previously published work, with modifications tailored to the specific requirements of this study.[26] For the determination of Al^{3+} in tomato paste samples, 5.0 g of the homogenized sample was weighed into PTFE vessels, and 10 mL of 69% HNO_3 and 5 mL of 36% HCl were added. The samples were digested using a microwave oven with a predefined program: the first stage involved a power of 1400 W, a ramp time of 10 minutes, a hold time of 10 minutes, and Fan setting 1; the second stage had a power of 0 W, a ramp time of 0 minutes, a hold time of 15 minutes, and Fan setting 3. After digestion, the samples were diluted to a final volume of 100 mL with ultrapure water. To remove interfering lipids, the solution was partitioned with hexane (3 × 20 mL), discarding the hexane layer and retaining the aqueous phase. Finally, the filtered aqueous solution was analyzed for aluminum content using the proposed method. Control samples were prepared by spiking tomatoes sauce, confirmed to be free of aluminum ions, with known concentrations of aluminum ions in glass bottles. Glassware was exclusively used to prevent potential aluminum ion contamination from plastic materials.

2.7. Canned tuna sample preparation for Co^{2+} determination

Canned tuna was obtained from a local supermarket, containing natural tuna preserved with water and salt, as indicated by the ingredient labels, without the addition of oils. Samples were collected from supermarkets in Assiut City, Egypt. After opening each can, the liquid was drained off, and the tuna meat was thoroughly homogenized using a food blender. The extraction procedure was adapted from a previously established method, with adjustments made to suit the unique conditions and objectives of this investigation.[3] 20.0 g of the homogenized fish muscle (wet weight) was accurately weighed and placed in a Teflon digestion vessel with 7 mL of concentrated nitric acid (65% HNO_3) and 1 mL of hydrogen peroxide (30% H_2O_2). The vessels were subjected to a microwave digestion program with two steps: (1) ramping the temperature from 25 °C to 200 °C over 10 minutes at 1000 W and (2) maintaining the temperature at 200 °C for an additional 10 minutes with 1000 W power. The digested samples were then diluted with ultrapure water to a volume of 25 mL in acid-washed standard flasks, filtered through paper filters. For cobalt ion recovery studies, 2 mL of the digested samples was spiked with different concentrations

of Co^{2+} solution, thoroughly shaken, and stored at 4 °C prior to measurements.

3. Results and discussion

3.1. Characterization of the prepared NSDC-dots

The transmission electron microscopy analysis revealed that these NSDC-dots exhibit excellent morphological characteristics. The TEM images (Fig. 1A) confirm the uniform spherical morphology of the nanoparticles, exhibiting excellent dispersion without noticeable aggregation. A comprehensive size analysis reveals well-defined dimensional characteristics, with nanoparticle diameters ranging from 2.3 to 6.0 nm. Gaussian distribution fitting yields an average size of 4.4 nm (Fig. 1A inset), indicating a highly uniform and narrow size distribution. XRD analysis revealed a prominent diffraction peak at 2θ = 24.45° (Fig. 1B), corresponding to the (001) crystal plane, a characteristic feature of the lattice structure in carbon-based nanomaterials.[27] The FTIR spectrum (Fig. 1C) identifies key functional groups, offering structural insights into NSDC-dots. The broad peak at 3433 cm^{-1} indicates the presence of O–H and N–H stretching vibrations, suggesting hydroxyl groups and primary/secondary amines on the surface.[28] The small peak at 2930 cm^{-1} can be attributed to C–H stretching of alkyl groups, while the sharp peak at 1717 cm^{-1} strongly suggests C=O stretching vibrations from carboxylic acid or carbonyl groups.[29] The peak at 1506 cm^{-1} corresponds to C=C aromatic ring stretching and N–H bending vibrations, reflecting the aromatic nature inherited from *o*-phenylenediamine precursor.[30] The peak at 1367 cm^{-1} likely represents C–N stretching vibrations, indicating the successful incorporation of nitrogen from both precursors. The peak at 1177 cm^{-1} can be assigned to C–O stretching and possibly C–S stretching from the cysteine precursor, while the small peak at 820 cm^{-1} typically corresponds to aromatic C–H out-of-plane bending vibrations.[31] Together, these peaks confirm the successful formation of carbon dots with surface functionalities from both precursors. XPS analysis elucidates the elemental composition and bonding environments of the carbon dots. The survey spectrum reveals the presence of four primary elements through their characteristic binding energies: carbon (286.66 eV), nitrogen (402.42

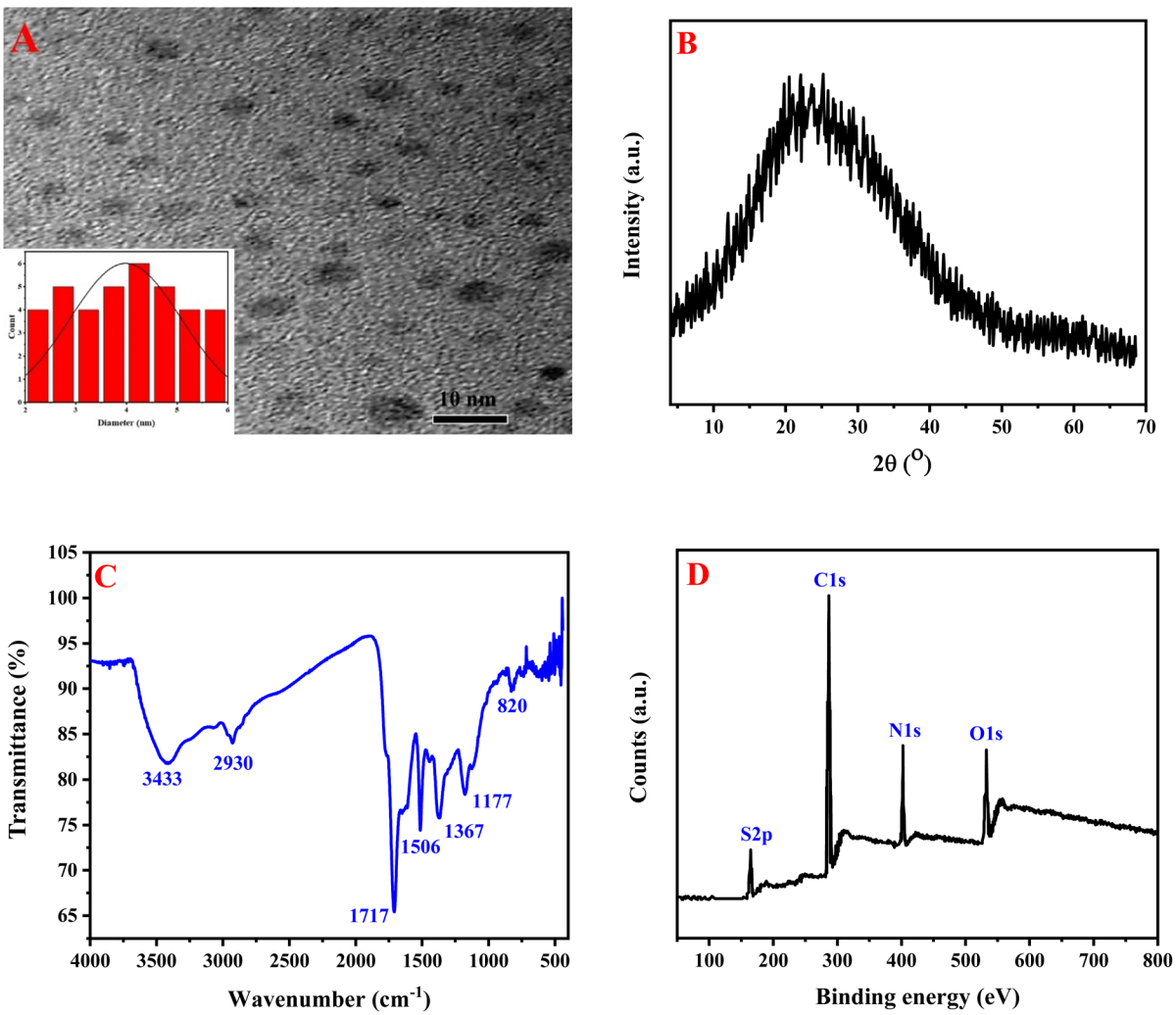

Fig. 1 (A) TEM image (inset: size distribution histogram), (B) XRD pattern, (C) FTIR spectrum, and (D) XPS spectrum of NSDC-dots.

eV), oxygen (533.24 eV), and sulfur (168.54 eV), confirming successful incorporation of these elements in the carbon dot structure (Fig. 1D). A detailed examination of the C 1s spectrum shows four distinct chemical environments: sp^2 carbon and C–C bonds (284.98 eV), C–N/C–O bonds (285.87 eV), C═O groups (287.31 eV), and carboxyl groups (O–C═O) at 289.04 eV, indicating a complex carbon framework with various functional groups (Fig. 2A). The S 2p XPS spectrum reveals two characteristic peaks at 169.22 eV and 170.32 eV, representing the S $2p_{3/2}$ and S $2p_{1/2}$ spin–orbit coupling components of sulfur atoms in a single chemical environment (Fig. 2B). The O 1s spectrum demonstrates two oxygen environments: one at 531.84 eV corresponding to C═O bonds and another at 533.14 eV representing C–O bonds and/or sulfonic acid groups (Fig. 2C). The N 1s spectrum reveals two distinct nitrogen environments: pyrrolic or amine nitrogen (400.05 eV) and graphitic or quaternary nitrogen (401.76 eV), indicating successful nitrogen doping into the carbon dot structure through different bonding configurations (Fig. 2D).[16] This comprehensive XPS analysis confirms the formation of highly functionalized carbon dots with multiple heteroatom dopants in various chemical states.

3.2. Spectroscopic characterization of NSDC-dots

Spectroscopic analysis highlights the distinctive photophysical properties of the synthesized carbon dots. The peak at 232 nm corresponds to π–π* transitions of C═C bonds in the sp^2 carbon core. The peaks at 275 nm and 289 nm indicate n–π* transitions involving nonbonding electrons from nitrogen and oxygen-containing functional groups. The peak at 337 nm suggests extended conjugated structures within the carbon dot framework.[32] The absorption at 419 nm is characteristic of surface state transitions, likely involving surface-bound functional groups and/or defect states that contribute to the fluorescence properties (Fig. 3A).[32] The fluorescence analysis demonstrates intriguing dual emission behavior, with two distinct peaks appearing at 403 nm and 532 nm when excited at 320 nm. The longer wavelength emission at 532 nm exhibits excitation-independent behavior across excitation wavelengths from 290–380 nm (Fig. 3B), suggesting it originates from surface state emissions, while the shorter wavelength peak at 403 nm shows excitation-dependent characteristics typical of core state emissions.[33] Both peaks demonstrate varying intensities with changing excitation wavelengths, and 320 nm was strategically selected as the optimal excitation wavelength as it provides

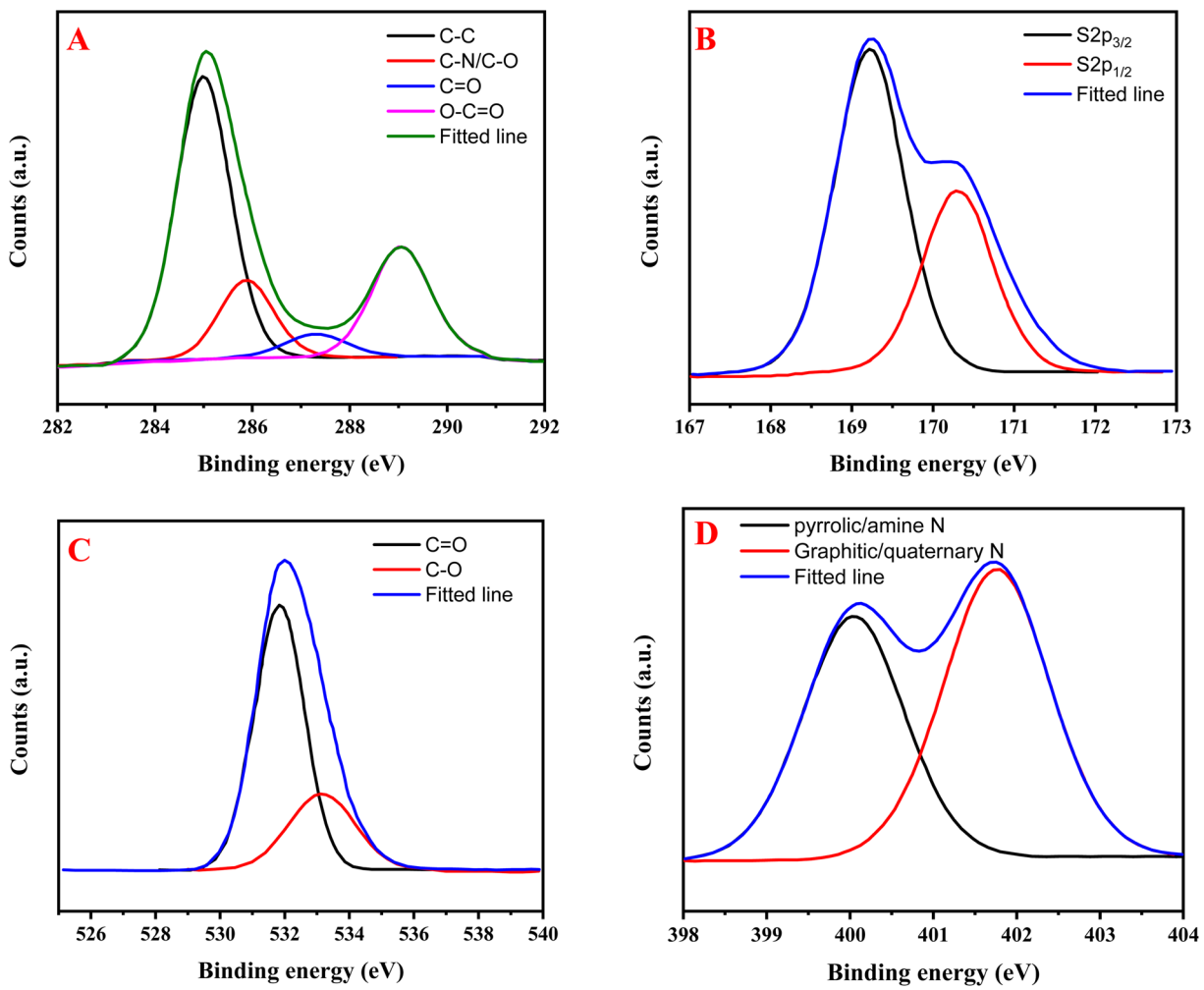

Fig. 2 XPS spectra of NSDC-dots, showcasing (A) C 1s, (B) N 1s, (C) O 1s, and (D) S 2p regions.

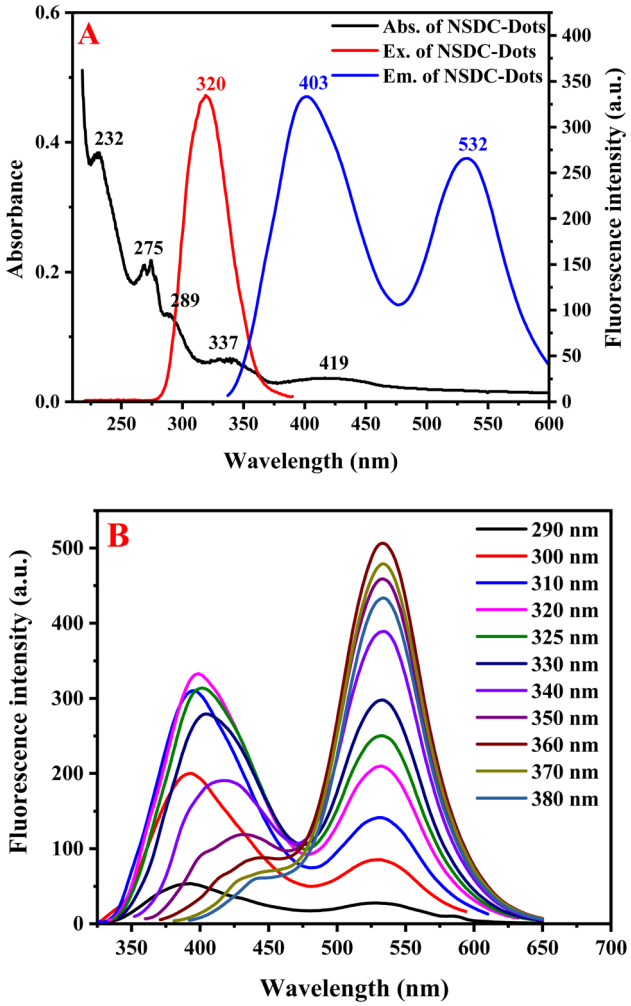

Fig. 3 (A) UV-vis absorption spectra, fluorescence and excitation spectra of NSDC-dots. (B) Fluorescence emission spectra of NSDC-dots after exposing to different excitation wavelengths ranging from 290 to 380 nm.

balanced intensity for both emission peaks. The relatively high quantum yield of 18.95% indicates efficient fluorescence emission, making these carbon dots promising candidates for various sensing and imaging applications.

3.3. Stability of NSDC-dots

Various stability parameters were systematically investigated for the prepared NSDC-dots using their characteristic dual emission property, monitored through the fluorescence intensity ratio (F_{403}/F_{532}). The pH stability studies indicated that the fluorescence ratio exhibited maximum values under acidic conditions, followed by a gradual decline with increasing pH values (Fig. S1A†). The carbon dots demonstrated exceptional stability across varying ionic environments, maintaining consistent fluorescence responses over a broad NaCl concentration range (0.01–1.0 M) (Fig. S1B†). Photobleaching resistance was assessed *via* extended UV irradiation (365 nm, 300 min), demonstrating excellent photostability with minimal fluorescence degradation (Fig. S1C†). Thermal stability analysis showed that the fluorescence properties remained unaffected within the temperature range of 20–80 °C, although notable changes in emission characteristics were observed when the temperature exceeded 60 °C (Fig. S1D†).

3.4. Optimization of metal ion detection conditions

The optimization studies for metal ion detection using NSDC-dots were conducted by monitoring the relative fluorescence intensity ratio (F/F_0), where F represents the fluorescence response after metal ion addition and F_0 indicates the initial fluorescence of carbon dots. Firstly, the pH-dependent behavior revealed fascinating mechanistic insights for each metal ion interaction (Fig. S2A†). For cobalt ions, the optimal response at neutral pH 7 suggests that the metal-binding sites on the carbon dot surface are most accessible when functional groups like carboxylates are partially deprotonated, creating favorable electrostatic conditions for Co^{2+} coordination. In contrast, aluminum ions showed enhanced binding under acidic conditions (pH 3–5), which can be attributed to the strong preference of Al^{3+} for oxygen-containing ligands and its tendency to form stable complexes in acidic media where it exists predominantly as the free Al^{3+} ion rather than hydroxide species. Secondly, the kinetic investigation demonstrated remarkably fast interaction dynamics, with stable signal achievement within just one minute, indicating that the surface functional groups of the carbon dots are highly accessible, and the binding sites are well-oriented for rapid metal ion complexation (Fig. S2B†). This rapid response time, combined with the distinct pH preferences, suggests different binding mechanisms for Co^{2+} and Al^{3+}, making these carbon dots excellent candidates for selective dual-ion sensing applications.

3.5. Ratiometric fluorescence detection of Al^{3+}/Co^{2+} based on NSDC-dots

Sensitivity studies demonstrated the remarkable dual-sensing capability of NSDC-dots for Co^{2+} and Al^{3+} ions *via* distinct fluorescence responses. For Co^{2+} detection, increasing concentrations (0–0.7 μM) selectively enhanced the 403 nm emission peak, while the 532 nm peak remained relatively stable (Fig. 4A). This selective response enabled construction of a ratiometric calibration curve (F_{403}/F_{532}) that showed excellent linearity in the range of 0–0.7 μM (Fig. 4A inset), following the equation $F_{403}/F_{532} = 1.82[Co^{2+}] + 1.61$ ($R^2 = 0.9946$). The method demonstrated high sensitivity with a detection limit of 0.012 μM, calculated using the standard $3\sigma/s$ criterion. Conversely, Al^{3+} sensing exhibited a complementary response, where increasing Al^{3+} concentrations (0–1.6 μM) progressively enhanced the 532 nm emission, while the 403 nm peak remained unchanged (Fig. 4B). The ratiometric response (F_{532}/F_{403}) displayed linear correlation with Al^{3+} concentration (Fig. 4B inset), following the equation $F_{532}/F_{403} = 0.41[Al^{3+}] + 0.75$ with an impressive correlation coefficient of 0.9971. The analytical performance for aluminum detection achieved a detection limit of 0.06 μM based on the $3\sigma/s$ calculation. These distinct ratiometric responses, with different peaks being enhanced for each metal ion, demonstrate the sensor's

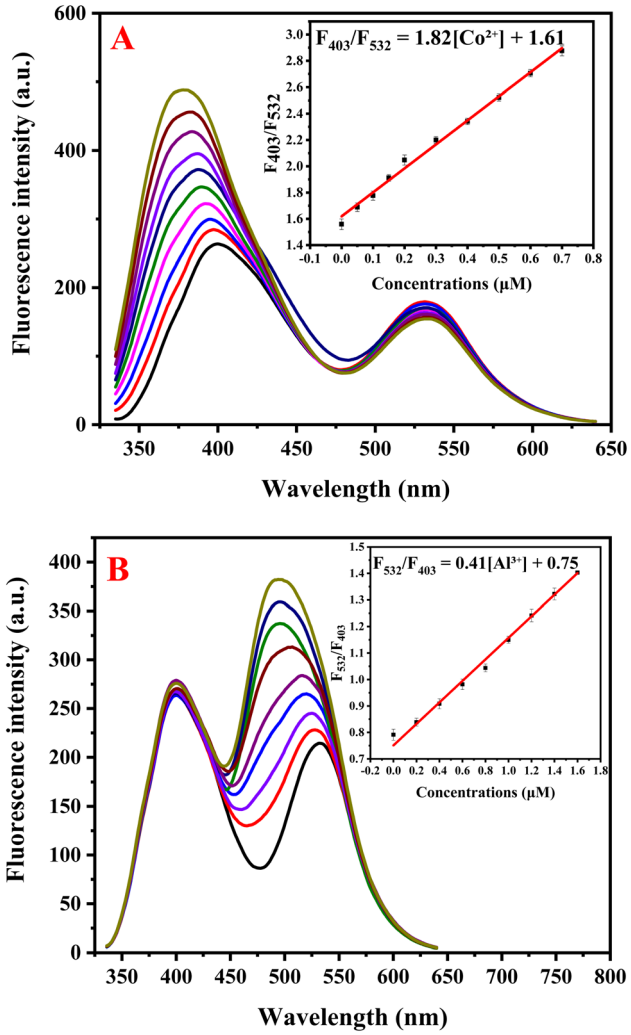

Fig. 4 (A) Fluorescence spectra of NSDC-dots with Co^{2+} concentration range 0–0.7 μM. The figure inset shows linear relationship between the fluorescence intensity ratio (F_{403}/F_{532}) and the Co^{2+} concentration. (B) Fluorescence spectra of NSDC-dots with Al^{3+} concentration range 0–1.6 μM. The figure inset shows linear relationship between the fluorescence intensity ratio (F_{532}/F_{403}) and the Al^{3+} concentration.

capability for selective dual-ion detection with impressive sensitivity, surpassing that of most reported methods as evidenced by the comparative data presented in Tables 1 and 2.

The proposed method demonstrates the capability for the successful simultaneous determination of both aluminum and cobalt ions, in case of the presence of both ions in matrices such as environmental water (Fig. S3†), highlighting an additional advantage of the method for broader analytical applications.

3.6. Selectivity study

The robustness of the NSDC-dots-based ratiometric fluorescence sensing probe was thoroughly validated through comprehensive interference studies to ensure its reliability under real-world analytical conditions. The probe's selectivity was tested against a wide range of molecular interferants

Table 1 Comparison of this study with existing fluorescent probes for Co^{2+} sensing

Method	Linearity range (μM)	Detection limit (μM)	Ref.
N,S-GQDs	0–40	1.25	34
CDs	1–961	0.097	35
$CuInS_2$/ZnS/TGA QDs	0.3–90.4	0.16	36
TGA CdS QDs	0.5–80	0.05	37
P,N-CQDs	0–60	0.053	38
TPTZ-CDs	0.4–50	0.234	39
N,S-CDs	0.08–100	0.08	40
Amplex UltraRed	0.045–1	0.014	41
N,S-CDs	0–40	2.64	28
N,Cl-CDs	0.1–70	0.03	42
NSDC-dots	0–0.7	0.012	This work

commonly found in food matrices, including sugars (glucose, sucrose, fructose), amino acids (glycine, histidine, cysteine), organic acids (citric acid, ascorbic acid, lactic acid, benzoic acid), and artificial sweeteners (saccharin), all at concentrations of 10.0 μM (Fig. S4†). Despite the presence of these interferants, the probe exhibited a strong and specific ratiometric response for cobalt ions (detected at 403 nm) and aluminum ions (detected at 532 nm), with minimal interference. Additionally, the probe's resilience was confirmed through an ionic interference study, where it demonstrated excellent stability in the presence of physiologically relevant metal cations and anions (*e.g.*, Cu^{2+}, Fe^{3+}, Zn^{2+}, Mn^{2+}, Ni^{2+}, Cr^{3+}, Na^{+}, K^{+}, Mg^{2+}, Ca^{2+}, Fe^{2+}, Sn^{2+}, Cl^{-}, SO_4^{2-}, PO_4^{3-}, NO_3^{-}) at the same concentration. This dual validation approach—testing both molecular and ionic interferants—highlighted the probe's exceptional selectivity and ability to accurately quantify Co^{2+} and Al^{3+} in complex food matrices, establishing it as a reliable and precise analytical tool for real-world applications.

3.7. Mechanism for detection of Al^{3+} and Co^{2+}

The differential fluorescence response of the dual-emission carbon dots (403 nm and 532 nm) to cobalt (Co^{2+}) and aluminum (Al^{3+}) ions can be attributed to their distinct interaction mechanisms with the carbon dot surface, which is rich in heteroatoms (N, S, and O) and functional groups such as $-NH_2$, –COOH, and –SH. The carbon dots, synthesized from cysteine and *o*-phenylenediamine (OPD), possess two emissive centers corresponding to nitrogen and sulfur-rich regions, resulting in characteristic fluorescence at 403 nm and 532 nm.

The response mechanism is governed by the unique coordination chemistry of Co^{2+} and Al^{3+}, as well as their specific interactions with functional groups on the carbon dots. Cobalt ions, being intermediate Lewis's acids, preferentially interact with nitrogen and sulfur-containing groups, such as $-NH_2$ and –SH. These interactions stabilize the nitrogen-rich domains likely derived from OPD, reducing non-radiative recombination pathways and enhancing fluorescence at 403 nm.[53] This enhancement may also involve surface passivation or electron delocalization, leading to structural rigidification in nitrogen-doped regions.[54] In contrast, aluminum ions, as hard Lewis

Table 2 Comparison of this work with other reported fluorescent probes for the detection of Al^{3+}

Method	Linearity range (μM)	Detection limit (μM)	Ref.
B,N@CDs	0–100	1.07	43
Lithium organic framework	10–500	4	44
β-Cyclodextrin–N@CDs	0–20	0.231	45
N@CDs	0.1–5.5	0.0097	46
Amino acid@CDs	1–20	0.32	47
2-Hydroxynaphthalene based acyl hydrazone	0–1.8	0.0422	48
N@CDs	10–2500	0.023	49
CDs	5–550	0.695	50
N@CDs	0–500	0.216	51
1-(2-Pyridylazo)-2-naphthol	1.0–5.0	0.018	52
NSDC-dots	0–1.6	0.06	This work

acids, exhibit a strong preference for oxygen-rich groups like –COOH and hydroxyls, as well as sulfur moieties. The binding of Al^{3+} to these groups induces significant changes in the surface states, possibly restricting molecular motion through aggregation-induced emission (AIE).[55] Furthermore, the strong vibration of the S–S bond in the synthesized NSDC-dots consumes the energy of the excited state, resulting in their nearly non-fluorescent behavior.[46] However, the addition of Al^{3+} disrupts this vibrational state, restoring fluorescence. This leads to fluorescence enhancement at 532 nm, as the aluminum interactions favor the stabilization of the sulfur and oxygen-rich regions derived from cysteine.[56]

The Hard–Soft Acid–Base (HSAB) theory further supports this selectivity,[57] where Co^{2+} prefers intermediate binding sites (N and S), and Al^{3+} strongly favors hard bases (O and S). Additionally, differences in ionic size, charge density, and binding affinity contribute to their selective interactions. Co^{2+} interactions promote electron transfer and localized structural rigidity, enhancing short-wavelength emission (403 nm), while Al^{3+} binding induces surface polarization and structural stabilization of long-wavelength emitters (532 nm).

The differential response of the dual-emission carbon dots to aluminum and cobalt ions can be attributed to their distinct interactions with the carbon dot surface, as reflected in the UV-Vis and fluorescence spectra. For Al^{3+}, a red shift in the UV-Vis absorption peak at 419 nm, coupled with an increase in intensity, indicates strong coordination with oxygen-rich groups (–COOH and –OH), likely causing significant electronic redistribution and aggregation (Fig. 5A). The more pronounced spectral changes for Al^{3+} suggest macroscopic structural alterations, including aggregation, which are further supported by a blue shift in fluorescence, likely due to aggregation-induced emission (AIE) and surface rigidification. The increase in absorbance may be attributed to particle aggregation, which can simultaneously absorb and scatter the incident light source. In contrast, Co^{2+} does not alter the intensity of the peak at 419 nm but induces a new absorption peak at 515 nm (Fig. 5B), indicative of localized complex formation with nitrogen and sulfur groups ($–NH_2$ and –SH). This interaction stabilizes specific electronic transitions without causing significant aggregation, as confirmed by the absence of major shifts in the original UV-Vis peak. The fluorescence blue shift observed for both ions suggests structural rigidification or changes in electron density, with Al^{3+} primarily driving macroscopic aggregation and Co^{2+} promoting localized stabilization and new emission pathways (Fig. 4A and B). These distinct behaviors underpin the selective enhancement of emission at 532 nm for Al^{3+} and at 403 nm for Co^{2+}.

The TEM imaging reveals differential aggregation behavior that provides crucial insights into the distinct interaction mechanisms of Al^{3+} and Co^{2+} with the NSDC-dots.[58] The more pronounced aggregation observed with aluminum ions can be attributed to its higher charge density and stronger tendency to form bridging interactions as a hard Lewis acid (Fig. 5C). Al^{3+} likely promotes extensive cross-linking between multiple carbon dots through simultaneous coordination with oxygen-containing groups (carboxylates and hydroxyls) on different particles, leading to the formation of larger aggregated clusters. This extensive aggregation correlates well with the significant changes observed in the UV-visible spectrum and the enhancement of the 532 nm emission peak. In contrast, cobalt ions show limited aggregation in TEM images (Fig. 5D), suggesting a different interaction mechanism where Co^{2+} forms more localized, discrete coordination complexes primarily with nitrogen-containing regions derived from OPD. This selective binding results in the appearance of a new absorption peak at 515 nm and enhancement of the 403 nm emission without extensive inter-particle crosslinking. These distinct aggregation patterns further support the dual-sensing mechanism where different metal ions interact preferentially with specific regions of the carbon dots, leading to unique spectroscopic responses.

Dynamic light scattering measurements revealed that the synthesized carbon dots exhibit excellent dispersity in aqueous medium with a narrow size distribution and hydrodynamic diameter centered around 4.4 nm (Fig. 1A). Upon interaction with metal ions, distinct changes in particle size were observed – aluminum ions induced significant aggregation resulting in larger hydrodynamic diameters (reaching approximately 17.7 nm) with broader size distribution (Fig. 5C inset), indicating formation of extensive particle aggregates. In contrast, cobalt ion addition led to a relatively modest increase in hydrodynamic diameter (around 13.3 nm) (Fig. 5D inset), suggesting

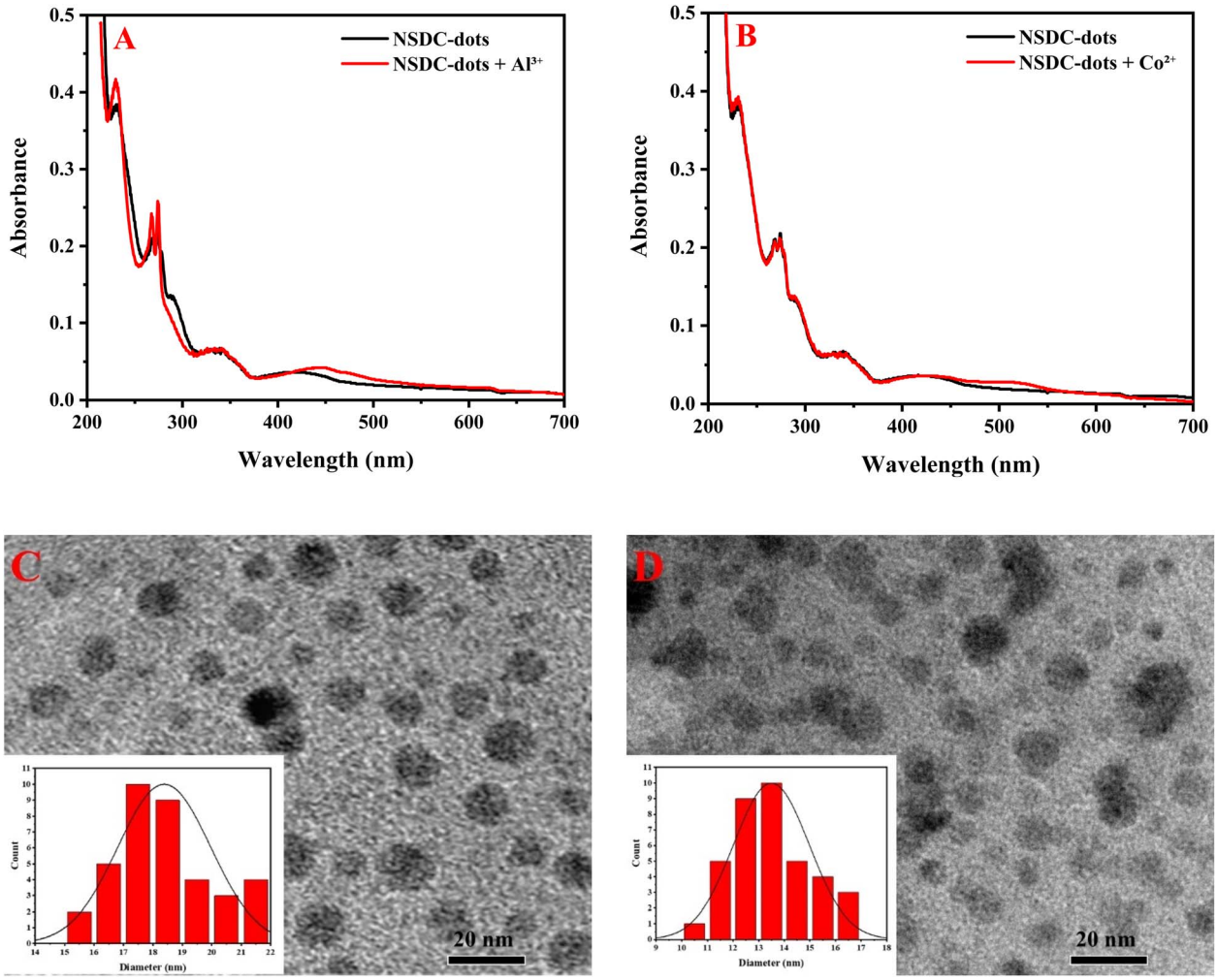

Fig. 5 UV-vis absorption spectra of (A) NSDC-dots + Al^{3+}, (B) NSDC-dots + Co^{2+}, and TEM images of (C) NSDC-dots + Al^{3+}, (D) NSDC-dots + Co^{2+}.

more limited inter-particle interactions. These findings align with the TEM observations and support the proposed differential binding mechanisms, where Al^{3+} promotes extensive cross-linking while Co^{2+} forms more discrete coordination complexes with the carbon dots.

The fluorescence lifetime results reveal distinct interaction mechanisms for Co^{2+} and Al^{3+} with the carbon dots. Co^{2+} induces a moderate lifetime increase due to localized binding with nitrogen and sulfur groups, stabilizing emissive states and forming a new emission at 515 nm (Fig. S5†). In contrast, Al^{3+} causes a significant lifetime increase (Fig. S5†), driven by strong binding with oxygen-rich groups and aggregation-induced emission (AIE), which restricts molecular motion and enhances excited-state stabilization. These differences underscore the localized effects of Co^{2+} and the aggregation-driven effects of Al^{3+} on fluorescence properties.

3.8. Application of the proposed method to canned foods

The analytical performance of the developed fluorometric method was rigorously evaluated through comprehensive recovery studies in complex food matrices. The method validation focused on two challenging sample types: canned tuna for cobalt determination and canned tomato sauce for aluminum quantification. Standard addition methodology was employed to assess potential matrix effects and method accuracy, with each sample fortified at three distinct concentration levels. The recovery data demonstrated exceptional accuracy, with aluminum recoveries ranging from 97.50–100.67% and cobalt recoveries spanning 97.01–98.02%. The % recovery is calculated using the formula: recovery (%) = ((found concentration − initial concentration)/added concentration) × 100. Method precision was evaluated through replicate analyses (n = 3), yielding relative standard deviation (RSD) values below 3.13% and 3.12% for aluminum and cobalt determinations, respectively (Table 3). These analytical figures of merit – particularly the near-quantitative recoveries and low RSD values – indicate minimal matrix interference and robust method performance. The statistical parameters underscore the method's reliability for accurate quantification of both metal ions in complex food matrices, with precision and accuracy well within acceptable analytical criteria for trace metal analysis in food samples. The validated method thus presents a reliable

Table 3 Results of the analysis of canned tomato and canned tuna samples ($n = 3$)

Sample	Added (μM)	Found (μM)	Recovery%	RSD%
Canned tomato	0	0.185	—	—
	0.2	0.381	98.00	2.82
	0.4	0.575	97.50	2.58
	0.6	0.789	100.67	3.13
Canned tuna	0	0.054	—	—
	0.05	0.101	98.02	3.12
	0.1	0.152	97.01	2.89
	0.15	0.201	97.33	2.98

analytical tool for monitoring metal ion leaching in canned food products, with performance characteristics suitable for routine quality control applications. The proposed method is well-suited for determining aluminum in canned tomato sauce and cobalt in canned tuna. Its range of 0.2 to 1.6 μM for aluminum (5.4 to 43.2 mg kg^{-1}) covers reported levels in canned tomatoes (1–20 mg kg^{-1}),[59] while its range of 0.05 to 0.7 μM for cobalt (0.003 to 0.041 mg kg^{-1}) aligns with typical cobalt levels in canned tuna (0.01–0.1 mg kg^{-1}).[2] This ensures accurate and sensitive quantification for both metal ions in their respective food matrices.

3.9. Effect of different storage condition on Al^{3+} and Co^{2+} levels in canned foods

The migration of aluminum from cans into tomato sauce likely follows a complex pattern influenced by both storage time and temperature. Under standard storage conditions (25 °C), aluminum levels increased from initial concentrations of around 0.5 mg kg^{-1} to approximately 3.0 mg kg^{-1} after 6 months and potentially reaching 6.0 mg kg^{-1} after 12 months. This time-dependent increase occurs because the acidic nature of tomatoes (pH ~4.0–4.5) continuously promotes aluminum leaching through corrosion of the can's interior surface. When considering temperature effects, storing these cans at elevated temperatures (40 °C) would significantly accelerate this migration process – aluminum levels reach 4.0 mg kg^{-1} within just 6 months and potentially exceed 9.0 mg kg^{-1} after 12 months at this higher temperature. This enhanced migration at higher temperatures can be explained by both increased chemical reaction rates and potential physical changes in the protective oxide layer of the can's surface. The relationship between temperature and aluminum migration isn't simply linear – higher temperatures not only speed up the chemical interactions between the acidic tomato sauce and the aluminum surface but also might compromise the integrity of any protective coatings, leading to exponentially higher migration rates. This temperature-dependent behavior becomes particularly relevant in regions with warmer climates or in situations where canned products might be stored in non-climate-controlled conditions.

The migration of cobalt ions into canned tuna shows more subtle patterns compared to aluminum migration, primarily due to the different chemical environment and interaction mechanisms. At standard storage conditions (25 °C), cobalt levels increased modestly from initial concentrations of 0.02 mg kg^{-1} (natural content in tuna) to approximately 0.06 mg kg^{-1} after 6 months, potentially reaching 0.12 mg kg^{-1} after 12 months. This gradual increase reflects both the natural cobalt content in tuna tissue and the slower migration from packaging materials, influenced by factors like the salt content and any acidic components in the packing medium. Temperature plays a crucial role in this migration process – at elevated storage temperatures (40 °C), the cobalt levels might accelerate to reach 0.09 mg kg^{-1} within 6 months and potentially rise to 0.20 mg kg^{-1} after 12 months. This temperature-dependent increase can be attributed to enhanced metal mobility and potential changes in protein–metal binding interactions within the tuna matrix at higher temperatures. The more moderate increase in cobalt levels compared to aluminum in tomatoes reflects the less aggressive chemical environment in tuna (higher pH, less acidic), as well as the different mechanisms of metal migration from the packaging materials. These patterns become particularly significant for quality control in warehouses and distribution centers where temperature fluctuations might occur.

4. Conclusions

In this study, we have successfully developed and validated a novel ratiometric fluorometric sensor based on carbon dots for the quantification of aluminum and cobalt ions in canned food products. The sensor exhibits a distinctive dual-emission response, with separate fluorescence peaks at 403 nm and 532 nm corresponding to cobalt and aluminum ions, respectively. This selective response highlights the effectiveness of rational sensor design, utilizing distinct metal–ligand interactions on the carbon dot surface. Through extensive characterization and mechanistic studies, we have established a clear understanding of the underlying principles governing these selective responses. The method's exceptional analytical performance positions it as a valuable tool for food safety analysis. Furthermore, the successful application of this sensing probe to real-world samples of canned tomato sauce and tuna, achieving high recovery rates and excellent selectivity, validates its practical utility in complex food matrices. This work not only advances the field of metal ion sensing but also provides a reliable analytical solution for food safety monitoring. The simplicity, sensitivity, and dual-detection capability of our method make it a promising candidate for routine analysis in food quality control laboratories. Future research directions could explore the adaptation of this sensing probe for other metal ion pairs and its potential integration into portable testing devices for on-site analysis.

Data availability

Data will be available on request.

Conflicts of interest

There are no conflicts to declare.

Acknowledgements

The authors would like to extend their sincere appreciation to the Researchers Supporting Project, King Saud University, Riyadh, Saudi Arabia for funding this work through the project number (RSP2025R457).

References

1 T. Stahl, H. Taschan and H. Brunn, *Environ. Sci. Eur.*, 2011, **23**, 37.
2 G. Kowalska, U. Pankiewicz and R. Kowalski, *J. Anal. Methods Chem.*, 2020, **2020**, 2148794.
3 S. Mol, *J. Food Compos. Anal.*, 2011, **24**, 66–69.
4 S. P. Joshi, R. B. Toma, N. Medora and K. O'Connor, *Food Chem.*, 2003, **83**, 383–386.
5 R. Lauwerys and D. Lison, *Sci. Total Environ.*, 1994, **150**, 1–6.
6 R. Bonfiglio, M. Scimeca and A. Mauriello, *Arch. Toxicol.*, 2023, **97**, 2997–2998.
7 G. R. Lyles and F. B. Dowling, *Anal. Chim. Acta*, 1963, **29**, 489–499.
8 R. F. Sanzolone, T. T. Chao and G. L. Crenshaw, *Anal. Chim. Acta*, 1979, **105**, 247–253.
9 J. L. Fabec and M. L. Ruschak, *Anal. Chem.*, 1983, **55**, 2241–2246.
10 S. Capiau, E. Bolea-Fernandez, L. Balcaen, C. Van Der Straeten, A. G. Verstraete, F. Vanhaecke and C. P. Stove, *Talanta*, 2020, **208**, 120055.
11 I. M. Isa, S. N. A. Dahlan, N. Hashim, M. Ahmad and S. A. Ghani, *Int. J. Electrochem. Sci.*, 2012, **7**, 7797–7808.
12 J. Masac, J. Lovic, E. Beinrohr and F. Cacho, *Microchem. J.*, 2021, **164**, 106058.
13 A. L. P. Silvestre, M. I. Milani, E. L. Rossini, L. Pezza and H. R. Pezza, *Spectrochim. Acta, Part A*, 2018, **204**, 432–435.
14 D. Xu, H. Chen, Q. Lin, Z. Li, T. Yang and Z. Yuan, *RSC Adv.*, 2017, **7**, 16295–16301.
15 A. Z. Alanazi, K. Alhazzani, A. M. Mahmoud, A.-M. B. H. Ali and M. M. El-Wekil, *Microchem. J.*, 2024, **199**, 110000.
16 A. Z. Alanazi, K. Alhazzani, A. M. Mostafa, J. Barker, H. Ibrahim, M. M. El-Wekil and A.-M. B. H. Ali, *Microchim. Acta*, 2024, **191**, 505.
17 A. M. Alaseem, K. Alhazzani, A. Z. Alanazi, S. M. Alsanad, O. A. Alkhamees, G. Alasiri, M. M. El-Wekil and A.-M. B. H. Ali, *Microchem. J.*, 2024, **201**, 110645.
18 A. M. Alaseem, K. Alhazzani, A. Z. Alanazi, S. M. Alsanad, O. A. Alkhamees, G. Alasiri, M. M. El-Wekil and A.-M. B. H. Ali, *Microchem. J.*, 2024, **207**, 111887.
19 K. Alhazzani, A. Z. Alanazi, A. M. Mostafa, J. Barker, M. M. El-Wekil and A.-M. B. H. Ali, *RSC Adv.*, 2024, **14**, 5609–5616.
20 K. Alhazzani, A. Z. Alanazi, A. M. Mostafa, J. Barker, H. Ibrahim, M. M. El-Wekil and A.-M. B. H. Ali, *Microchem. J.*, 2024, **204**, 111129.
21 K. Alhazzani, A. Z. Alanazi, A. M. Mostafa, J. Barker, H. Ibrahim, M. M. El-Wekil and A.-M. B. H. Ali, *Microchem. J.*, 2024, **204**, 111092.
22 A. M. Mahmoud, Y. S. Alqahtani, M. M. El-Wekil and A.-M. B. H. Ali, *J. Fluoresc.*, 2024, DOI: 10.1007/s10895-024-03737-2.
23 A. M. EL-SAYED and M. A. M. ALI, *Assiut Vet. Med. J.*, 2020, **66**, 1–20.
24 M. R. Hadiani, R. Farhangi, H. Soleimani, H. Rastegar and A. M. Cheraghali, *Food Addit. Contam.:Part B*, 2014, **7**, 74–78.
25 N. Boadi, J. Mensah, S. Twumasi, M. Badu and I. Osei, *Food Addit. Contam.:Part B*, 2012, **5**, 50–54.
26 I. N. Pasias, V. Papageorgiou, N. S. Thomaidis and C. Proestos, *Food Anal. Methods*, 2012, **5**, 835–840.
27 A. M. Mahmoud, Y. S. Alqahtani, M. M. El-Wekil and A.-M. B. H. Ali, *Anal. Methods*, 2024, **16**, 3287–3296.
28 Y. Zhang, N. Liu, J. Huang, S. Wang, T. Qing, P. Zhang and B. Feng, *J. Ind. Eng. Chem.*, 2024, **137**, 122–131.
29 A. Z. Alanazi, K. Alhazzani, H. Ibrahim, A. M. Mostafa, J. Barker, A. M. Mahmoud, M. M. El-Wekil and A.-M. B. H. Ali, *Spectrochim. Acta, Part A*, 2025, **325**, 125161.
30 K. Alhazzani, A. Z. Alanazi, H. Ibrahim, A. M. Mostafa, J. Barker, A. M. Mahmoud, M. M. El-Wekil and A.-M. B. H. Ali, *Food Chem.*, 2025, **463**, 141396.
31 S. T. Alsharif, A. M. Mahmoud, M. M. El-Wekil and A.-M. B. H. Ali, *Microchem. J.*, 2025, **208**, 112618.
32 Q. Zhao, W. Song, B. Zhao and B. Yang, *Mater. Chem. Front.*, 2020, **4**, 472–488.
33 H. Ding, X.-H. Li, X.-B. Chen, J.-S. Wei, X.-B. Li and H.-M. Xiong, *J. Appl. Phys.*, 2020, **127**, 231101.
34 W. Boonta, C. Talodthaisong, S. Sattayaporn, C. Chaicham, A. Chaicham, S. Sahasithiwat, L. Kangkaew and S. Kulchat, *Mater. Chem. Front.*, 2020, **4**, 507–516.
35 F. Yarur, J.-R. Macairan and R. Naccache, *Environ. Sci.: Nano*, 2019, **6**, 1121–1130.
36 L. Zi, Y. Huang, Z. Yan and S. Liao, *J. Lumin.*, 2014, **148**, 359–363.
37 W.-T. Li, H.-W. Chang, W.-C. Yang, C. Lo, L.-Y. Wang, V. F. Pang, M.-H. Chen and C.-R. Jeng, *Sci. Rep.*, 2018, **8**, 5593.
38 S. Liao, F. Zhu, X. Zhao, H. Yang and X. Chen, *Sens. Actuators, B*, 2018, **260**, 156–164.
39 R. Tabaraki, N. Sadeghinejad and A. Nateghi, *J. Fluoresc.*, 2018, **28**, 251–257.
40 Y. Chen, P. Shang, Y. Dong and Y. Chi, *Sens. Actuators, B*, 2017, **242**, 1210–1215.
41 C.-Y. Tsai and Y.-W. Lin, *Analyst*, 2013, **138**, 1232–1238.
42 R. Tabaraki and F. Nazari, *Spectrochim. Acta, Part A*, 2023, **300**, 122829.
43 X. Li, L. Zhao, Y. Wu, A. Zhou, X. Jiang, Y. Zhan and Z. Sun, *Spectrochim. Acta, Part A*, 2022, **282**, 121638.
44 L. Feng, G. Ren, S. Ding, F. Wang, W. Yang, Z. Liang and Q. Pan, *Appl. Organomet. Chem.*, 2019, **33**, e5044.
45 M. Yao, J. Huang, Z. Deng, W. Jin, Y. Yuan, J. Nie, H. Wang, F. Du and Y. Zhang, *Analyst*, 2020, **145**, 6981–6986.
46 S. Sooksin, V. Promarak, S. Ittisanronnachai and W. Ngeontae, *Sens. Actuators, B*, 2018, **262**, 720–732.
47 J. Xu, Y. Zang, F. Yan, J. Sun, Y. Zhang and C. Yi, *Particle*, 2021, **38**, 2100201.
48 Y. Liu, L. Zhang, L. Chen, Z. Liu, C. Liu and G. Che, *Spectrochim. Acta, Part A*, 2021, **248**, 119269.
49 C. Yan, L. Guo, X. Shao, Q. Shu, P. Guan, J. Wang, X. Hu and C. Wang, *Anal. Bioanal. Chem.*, 2021, **413**, 3965–3974.

50 A. Pandi and S. Chinnathambi, *Inorg. Chem. Commun.*, 2025, **172**, 113696.
51 X. Mei, D. Wang, L. Zhang, J. Li and C. Dong, *Luminescence*, 2021, **36**, 1469–1475.
52 V. K. Gupta, S. K. Shoora, L. K. Kumawat and A. K. Jain, *Sens. Actuators, B*, 2015, **209**, 15–24.
53 L. Sun, Y. Liu, Y. Wang, J. Xu, Z. Xiong, X. Zhao and Y. Xia, *Opt. Mater.*, 2021, **112**, 110787.
54 D. Ozyurt, M. A. Kobaisi, R. K. Hocking and B. Fox, *Carbon Trends*, 2023, **12**, 100276.
55 Q. Zhang, X. Li, L. Yu, L. Wang, Z. Wen, P. Su, Z. Sun and S. Wang, *J. Environ. Sci.*, 2025, **149**, 68–78.
56 W. Wei, J. Huang, W. Gao, X. Lu and X. Shi, *Chemosensors*, 2021, **9**, 25.
57 M. M. Jones and W. K. Vaughn, *J. Inorg. Nucl. Chem.*, 1978, **40**, 2081–2088.
58 K. Ohkubo, S. C. Menon, A. Orita, J. Otera and S. Fukuzumi, *J. Org. Chem.*, 2003, **68**, 4720–4726.
59 S. Sander, O. Kappenstein, I. Ebner, K. A. Fritsch, R. Schmidt, K. Pfaff and A. Luch, *PLoS One*, 2018, **13**, e0200778.